



Phase segregation and miscibility of TiO_x nanocomposites in Gd-doped ceria solid electrolyte material

Junying Li,^a Prahlad K. Routh,^{a*} Yuanyuan Li,^a Anna Plonka,^a Evgeniy Makagon,^b Igor Lubomirsky^{b*} and Anatoly Frenkel^{a,c*}

Received 10 March 2023

Accepted 20 April 2023

Edited by K. Kvashnina, ESRF – The European Synchrotron, France

Keywords: X-ray absorption spectroscopy; electro-chemo-mechanical effect; local structural disorder.

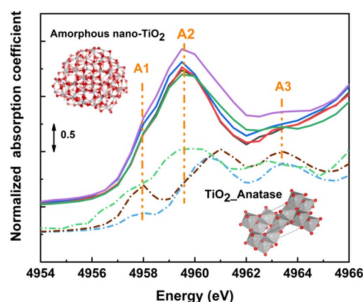
Supporting information: this article has supporting information at journals.iucr.org/s

^aDepartment of Materials Science and Chemical Engineering, Stony Brook University, Stony Brook, NY 11794, USA, ^bDepartment of Molecular Chemistry and Materials Science, Weizmann Institute of Science, Rehovot 761001, Israel, and ^cChemistry Division, Brookhaven National Laboratory, Upton, NY 11973, USA. *Correspondence e-mail: prahladkumar.routh@stonybrook.edu, igor.lubomirsky@weizmann.ac.il, anatoly.frenkel@stonybrook.edu

Electro-chemo-mechanical (ECM) coupling refers to mechanical deformation due to electrochemically driven compositional change in a solid. An ECM actuator producing micrometre-size displacements and long-term stability at room temperature was recently reported, comprising a 20 mol% Gd-doped ceria (20GDC), a solid electrolyte membrane, placed between two working bodies made of TiO_x /20GDC (Ti-GDC) nanocomposites with Ti concentration of 38 mol%. The volumetric changes originating from oxidation or reduction in the local TiO_x units are hypothesized to be the origin of mechanical deformation in the ECM actuator. Studying the Ti concentration-dependent structural changes in the Ti-GDC nanocomposites is therefore required for (i) understanding the mechanism of dimensional changes in the ECM actuator and (ii) maximizing the ECM response. Here, the systematic investigation of the local structure of the Ti and Ce ions in Ti-GDC over a broad range of Ti concentrations using synchrotron X-ray absorption spectroscopy and X-ray diffraction is reported. The main finding is that, depending on the Ti concentration, Ti atoms either form a cerium titanate or segregate into a TiO_2 anatase-like phase. The transition region between these two regimes with Ti(IV) concentration between 19% and 57% contained strongly disordered TiO_x units dispersed in 20GDC containing Ce(III) and Ce(IV) and hence rich with oxygen vacancies. As a result, this transition region is proposed to be the most advantageous for developing ECM-active materials.

1. Introduction

Electro-chemo-mechanical (ECM) coupling (Bishop *et al.*, 2014, 2017; Swallow *et al.*, 2014; Tuller & Bishop, 2011) generates large strain and dimensional changes in nanocomposites induced by the electrochemically driven compositional changes in the solid. Although the strain induced by the ECM effect is detrimental to Li-ion batteries (Sethuraman *et al.*, 2010; Swallow *et al.*, 2014; Wang *et al.*, 2015), the macroscopic strain resulting from the compositional changes across the device is attractive for an actuation mechanism. Swallow *et al.* (2017) demonstrated the first high-temperature (550°C), low-voltage ECM actuator. The induced strain was due to the mechanical response in $\text{Pr}_x\text{Ce}_{1-x}\text{O}_{2-\delta}$ (PCO) (δ is oxygen deficiency) films as a result of applied bias (Swallow *et al.*, 2017). However, the displacements produced were too small for practical use. The ECM-based actuator with a sandwich-like structure was recently fabricated by Makagon *et al.* (2021). It is able to produce micrometre-size displacements and long-term stability at room temperature. The key innovation behind this actuator that allowed it to operate at room



temperature is the use of the active layers (ActLs) made of the metal oxide/20 mol% Gd-doped ceria (20GDC) nanocomposites, serving as working bodies (WBs) (Makagon *et al.*, 2021, 2022) and separated by a micrometre-thick ionic conductor (IC) made of 20GDC, serving as a solid electrolyte (SE). After applying bias, oxygen ion transport through the IC electrolyte and the WBs undergo changes in volume upon oxidation or reduction, leading to the expansion in one ECM ActL and contraction in the other ECM ActL, inducing micrometre-sized displacement in the test structure (Makagon *et al.*, 2021).

Ti oxide/20GDC (Makagon *et al.*, 2022, 2021) (denoted as Ti-GDC for brevity) nanocomposites are found to be integral components functioning as WBs in ECM actuation. The local environment of the Ti species was reported to be a distorted TiO₆ octahedron in the case of 38% Ti in Ti-GDC (Li *et al.*, 2021). In addition, the dimensional changes under an external electric field were shown to be related to the ordering/disordering structural changes of the TiO₆ octahedron (Li *et al.*, 2021). To maximize the ECM response, we hypothesize that the formation of local TiO_x units should play an important role. Predicting the best composition for the ECM effect is difficult because Ti may incorporate in GDC differently, depending on the Ti concentration. Ti can either substitute for Ce atoms in the GDC lattice, form cerium titanates (*e.g.* Ce₂Ti₂O₇, Ce₂TiO₅, Ce₄Ti₉O₂₄, CeTiO₄ and CeTi₂O₆) (Preuss & Gruehn, 1994; Bazuev *et al.*, 1976; Otsuka-Yao-Matsuo *et al.*, 2004; Gionco *et al.*, 2013) or segregate into titania-rich phases. Therefore, studying the concentration-dependent structural changes in the Ti-GDC nanocomposites is essential for understanding and maximizing the mechanical deformation in the ECM actuator, which until now was designed exclusively by an Edisonian approach.

Although the local structure of Ti-GDC has not been systematically investigated to the best of our knowledge, the CeO₂-TiO₂ system has been studied in the past to some extent because of its promising applications as catalysts (Luo *et al.*, 2015), ferroelectric ceramics (Gao *et al.*, 2015) and electrodes (Kadhim *et al.*, 2021). Watanabe *et al.* (2009) characterized the crystalline phase and crystallite sizes of nanocrystalline TiO₂-CeO₂ mixed oxides (Ti_xCe_{1-x}O₂) by X-ray diffraction (XRD) and found that introducing a small amount of Ce ($x > 0.9$) into TiO₂ caused a structural distortion of the anatase phase. In contrast, introducing a small amount of Ti ($x < 0.3$) into CeO₂ caused a structural distortion of cubic fluorite phase (Watanabe *et al.*, 2009). However, when the fraction of TiO₂ was in the range between 0.5 and 0.7, their crystalline phase and crystallite sizes were not reported by XRD likely due to the too small sizes of the crystallites and enhanced structural disorder. The formation of Ce₂Ti₂O₇, containing ions of eightfold-coordinated Ce and sixfold-coordinated Ti, was detected by Raman spectroscopy and optical absorption in CeO₂-TiO₂ with 50 mol% CeO₂ (Gionco *et al.*, 2013). Because the tools for detecting and interpreting structural and compositional details on nanoscale (with dimensions less than ~3–5 nm) metal oxides are limited, X-ray absorption spectroscopy (XAS) stands out as the premier technique for this purpose (Rehr & Albers, 2000; Sayers *et al.*, 1971; Farges *et al.*,

1997; Frenkel *et al.*, 2002). X-ray absorption near-edge structure (XANES) is particularly sensitive to the local geometry of metal centers, providing information about the oxidation states and local symmetry, and not biased against structural disorder or hampered by nanoscale dimensions of materials (Rehr *et al.*, 1992; Rehr & Albers, 2000; Sayers *et al.*, 1971; Srivastava & Nigam, 1973; Ankudinov *et al.*, 2002). The pre-edge features in the XANES spectra in many cases contain key information about the electronic and structural properties of the local environment of metal oxides (Yamamoto, 2008; Srivastava & Nigam, 1973). Taking the Ti *K*-edge pre-edge features in the XANES spectra as an example, as shown by Farges *et al.* (1997), the pre-edge energy positions and signal intensities are well separated for fourfold-, fivefold- and sixfold-coordinated Ti for the Ti⁴⁺ species, although these results were obtained for standard compounds only. Theoretical modeling explained some of these trends and attributed the intensity of one of the pre-edge peaks to the square of the displacement of Ti atoms from the oxygen octahedral center (Poumellec *et al.*, 1991; Kraizman *et al.*, 1995). XAS has not been used for a systematic study of CeO₂-TiO₂ mixtures, although results obtained for several compositions of these mixtures were reported (Kityakarn *et al.*, 2013).

The objective of this study is to measure and understand the local structural environment around Ti in Ti-GDC over the broad Ti concentration range. For that, X-ray absorption spectroscopy was employed at both the Ti *K*-edge and Ce *L*₃-edge. Synchrotron-based X-ray diffraction was used as a complementary method to investigate the long-range structure of Ti-GDC at the same concentrations. To express the series of spectral changes in terms of the number of unique species present in the samples, principal component analysis of XANES spectra was used. As a result of the combined XAS, XRD and theoretical XANES modeling, we proposed the structures of the Ti-GDC system in each concentration region and identified the range of concentrations in which the strongest ECM effect is expected.

2. Experiment and data analysis

Nanocomposite thin films were fabricated according to the protocol developed by Makagon *et al.* (2021). In brief, Ti-GDC samples with various Ti concentrations were deposited by a magnetron co-sputtering method on SiO₂ substrates (around 280 μm) with a 100 nm Al adhesion layer. The samples are listed in Table S1 of the supporting information and are denoted as *x*% Ti-GDC, where *x* is the concentration of Ti. The deposition conditions are given in Table S1. XRD patterns of Ti-GDC samples were collected at beamline 28-ID-2 ($\lambda = 0.18456 \text{ \AA}$), National Synchrotron Light Source II (NSLS-II), Brookhaven National Laboratory, USA. XAFS data were collected at the Ti *K*-edge (4966 eV). X-ray absorption spectra of the Ti-GDC films were measured at beamline 8-BM of NSLS-II using a Si(111) double-crystal monochromator. The Ce *L*₃-edge was measured at beamline 4-3, Stanford Synchrotron Radiation Lightsource (SSRL), using a liquid-nitrogen-cooled Si(111) double-crystal mono-

chromator. All spectra were collected in fluorescence mode. The raw XAFS data were analyzed utilizing the *Athena* and *Artemis* interfaces of the *Demeter* software package (Ravel & Newville, 2005). The spectra were energy-aligned, merged and edge-step normalized. *FEFF* software (Rehr *et al.*, 2009; Rehr & Albers, 2000) was utilized to calculate the theoretical XANES spectra based on a specific structural model. Titanium oxide (III), Ti_2O_3 , was chosen as a standard to optimize the non-structural parameters.

3. Results and discussion

For the Ti *K*-edge XANES spectra of all Ti-GDC samples, as shown in Fig. S1 of the supporting information, the rising-edge positions are close to that of TiO_2 , suggesting that the oxidation state of Ti in all Ti-GDC samples is close to Ti^{4+} . The pre-edge feature A corresponds to the $1s$ to $3d$ transition in Ti and can be used for detecting and quantifying its off-center displacement (Frenkel *et al.*, 2005, 2007; Shanthakumar *et al.*, 2006). It appears, based on the calibration method developed by Farges *et al.* (1997), that, for all samples studied in Ti-GDC films with various Ti concentrations, Ti^{4+} predominantly coordinates with six oxygen atoms, as shown in Fig. 1. This conclusion and the caveats of the Farges' analysis and its applicability for nanoscale, non-bulk-like Ti–O compounds will be discussed below. In addition, for the Ce L_3 -edge XANES spectra of all Ti-GDC samples, as shown in Fig. S2, the rising-edge positions are close to that of 20GDC, suggesting that the oxidation states of Ce in all Ti-GDC samples are dominated by Ce^{4+} .

The variations in structural features can arise from either of the two possibilities. First, at each Ti fraction, a unique species with, correspondingly, unique spectral features is formed. Alternatively, a smaller number of species are formed over the entire concentration range, and the spectral changes

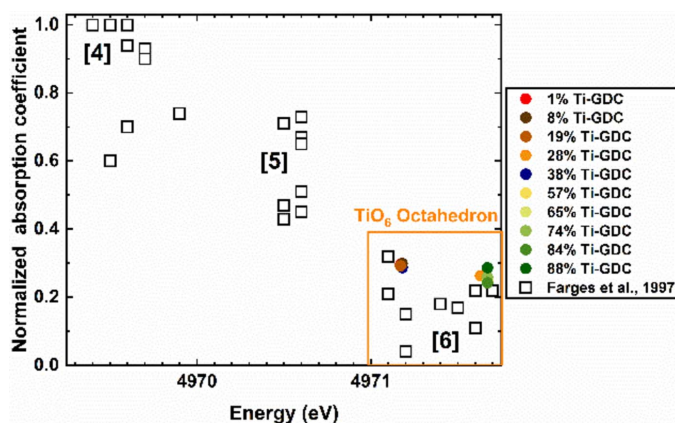


Figure 1 Normalized peak height versus energy position for Ti *K*-pre-edge features in XANES spectra of TiO_x units in different materials. There are three domains for fourfold-, fivefold- and sixfold-coordinated Ti {reproduced with permission from Farges *et al.* (1997) [Copyright 1997 American Physical Society]}. Colored symbols correspond to the Ti-GDC samples with different Ti concentrations. 38% Ti-GDC is reproduced from Li *et al.* (2021) with permission of the International Union of Crystallography.

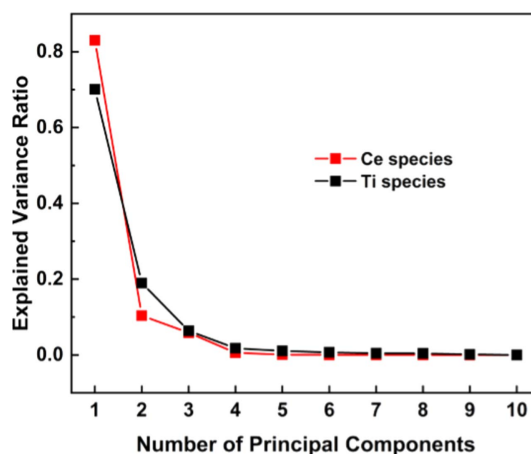


Figure 2 PCA scree plot for Ti species (black) for all Ti-GDC samples and Ce species (red) for all Ti-GDC and 20GDC samples.

reflect the differences in the mixing fractions of those few species. To group the samples based on the similarity of their spectral features, we employed principal component analysis (PCA) and obtained the number of groups contributing to this series of experimental spectra (Fay *et al.*, 1992). PCA is a multivariate analysis tool, which reduces the dimensionality of the dataset while preserving its covariance (Jolliffe & Cadima, 2016). PCA was applied on Ti *K*-edge and Ce L_3 -edge XANES spectra for all Ti-GDC samples (explained in Section S3). PCA scree plots for Ti (black) and Ce (red) species are shown in Fig. 2, indicating that the maximum number of sub-groups for both Ti and Ce species is three.

The two-dimensional principal subspace (Fig. 3) can be used to group the samples based on the cosine similarity scores (Fig. S3) obtained by analyzing Ti *K*-edge XANES spectra. Cosine similarity scores are defined as $\cos(\theta) = \mathbf{A} \cdot \mathbf{B} / \|\mathbf{A}\| \|\mathbf{B}\|$, where **A** (or **B**) refer to the vectors from the origin to the point of each sample in the principal subspace. Based on their cosine similarity score, XANES spectra are divided into three groups for Ti species: region I (1%, 8% and 19% Ti-GDC), transition region [28% Ti-GDC, 38% Ti-GDC reproduced from Li *et al.* (2021)] and region II (57%, 65%, 74%, 84% and 88% Ti-GDC). This grouping is consistent with the results obtained by Ce species, as shown in Figs. S4 and S5.

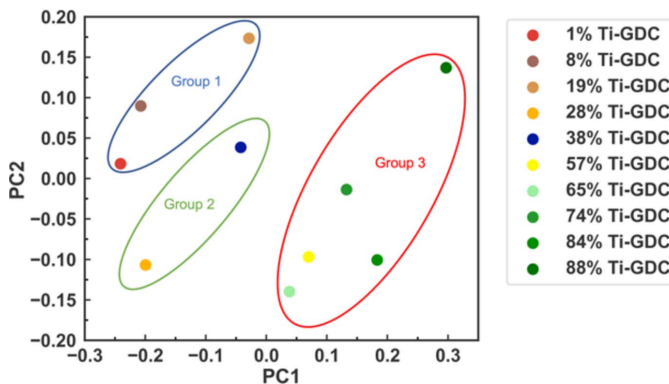


Figure 3 Two-dimensional principal subspace for Ti species. The species are grouped based on the similarity scores shown in Fig. S3.

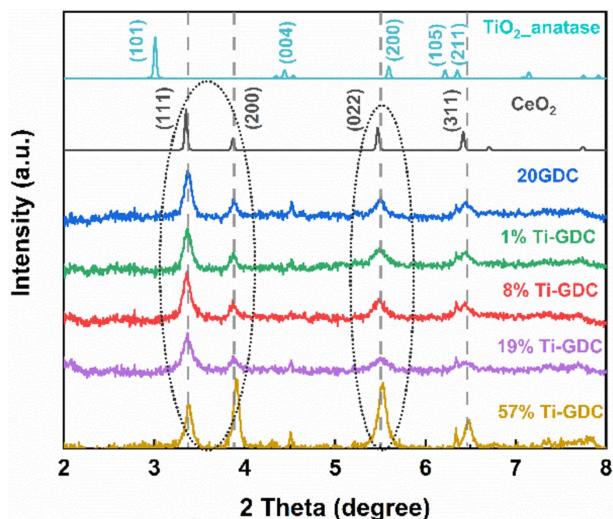


Figure 4
XRD pattern of the 20GDC, 1%, 8%, 19% (region I) and 57% Ti-GDC (region II) with reference fluorite CeO_2 and anatase TiO_2 calculated by VESTA software (Momma & Izumi, 2011).

To gain additional insight into the structural differences between the groups, we examined the XRD data. As shown in Fig. 4, it is apparent that fluorite CeO_2 is found in region I (1%, 8% and 19% Ti-GDC) and region II (57% Ti-GDC) via a series of (111), (200), (022) and (311) diffraction peaks. However, as shown in Fig. 4, the intensity of the (111) diffraction peak decreased, while the intensity of the (200) and (022) diffraction peaks increased in 57% Ti-GDC, indicating that interaction of Ti oxide with 20GDC distorted the CeO_2 lattice. The rest of the samples do not show any sharp peak features, as shown in Fig. S6, indicating that either ultra-small nanocrystals or amorphous structure would be formed in these Ti-GDC samples. In the following sections, we will describe the local structures of the samples in each region.

3.1. Region I

Based on the PCA-based grouping, region I contains 1%, 8% and 19% Ti-GDC samples. Several models can be proposed for the local environments of Ti. One such model (M1) is substitutional, in which Ti replaces the Ce atom in the cubic fluorite structure of CeO_2 . Another model is Ti forming local TiO_x -type structures, that correspond to region 3 (see below) and, hence, are excluded from consideration in the region I. The other models correspond to the known Ce–Ti–O stoichiometries with TiO_6 octahedra, namely M2 (CeTi_2O_6), M3 ($\text{Ce}_2\text{Ti}_2\text{O}_7$), M4 (Ce_2TiO_5) and M5 (CeTiO_3), as shown in Fig. 5. The key difference in the local structures of Ti and Ce atom environments in these phases is as follows. In M1, Ti is surrounded by eight oxygen atoms in a cubic TiO_8 unit. Ti is bonded to six oxygen atoms to form corner-sharing TiO_6 octahedra in CeTi_2O_6 (M2), and to form corner-sharing TiO_6 octahedra with six equivalent TiO_6 octahedra and edge-sharing with six equivalent CeO_8 in $\text{Ce}_2\text{Ti}_2\text{O}_7$ (M3). In Ce_2TiO_5 (M4), Ce is bonded to six oxygen atoms. In CeTiO_3 (M5), Ce is bonded to twelve oxygen atoms to form CeO_{12} , and Ti is coordinated with six oxygen atoms.

We expect that the changes in the local environments between models M1–M5 should be reflected in the corresponding changes in their Ti *K*-edge XANES spectra. EXAFS data at the Ti *K*-edge (Fig. S7) were theoretically analyzed. The fitting model included the Ti–O scattering path, and its parameters were: coordination number, correction to the bond length, its variance and the energy origin correction. The amplitude reduction factor was obtained by analysis of bulk anatase EXAFS data and fixed in the fitting of all Ti-GDC samples, which is a standard procedure. The data and fits are shown in Fig. S8. The fitting results are given in Table S2, which demonstrates that, in agreement with the XANES results already reported in our manuscript, the coordination number of Ti–O bonds is not consistent with the substitutional model (for which the Ti–O coordination number should be

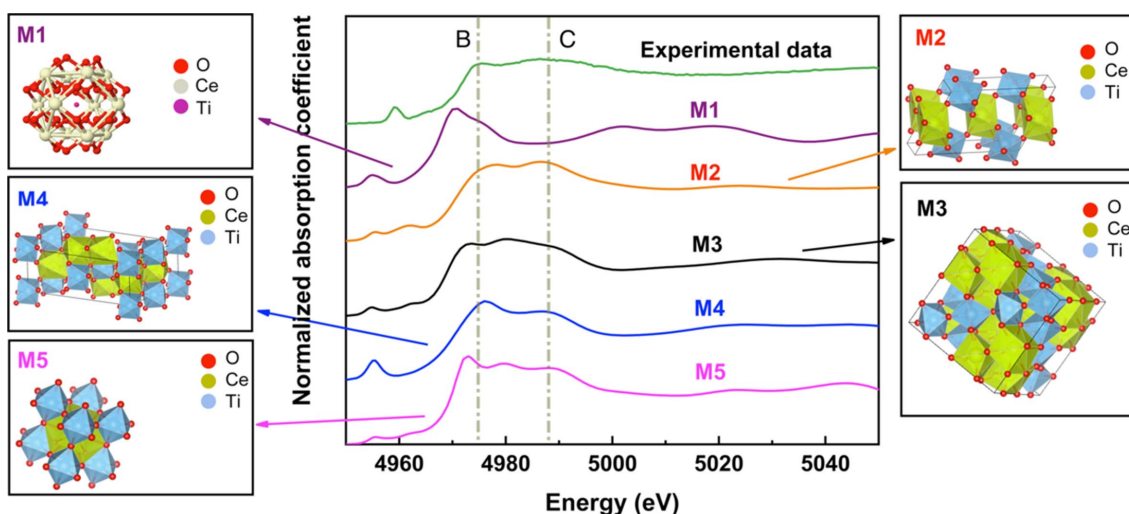


Figure 5
Experimental XANES spectra of Ti atoms in 8% Ti-GDC and simulated XANES spectra of Ti atoms in M1 (Ti replaces Ce in CeO_2), M2 (CeTi_2O_6), M3 ($\text{Ce}_2\text{Ti}_2\text{O}_7$), M4 (Ce_2TiO_5) and M5 (CeTiO_3). The structure files for M1–M5 were obtained from the Materials Project database (Petousis *et al.*, 2017; Munro *et al.*, 2020; Patel *et al.*, 2019; Jain *et al.*, 2013) and rendered using VESTA (Momma & Izumi, 2011).

equal to 8). A precise model of the Ti environment is not easy to glean from EXAFS analysis, due to the uncertainty in the amplitude factor obtained by EXAFS (0.6 ± 0.2) and the limited k -range (only the $2\text{--}9 \text{ \AA}^{-1}$ k -range could be used). In order to identify the possible structures of the Ti species, we performed theoretical XANES modeling. The experimental XANES spectrum of Ti_2O_3 , as shown in Fig. S9, was chosen as a standard to optimize the modeling (using *FEFF* code) parameters. The theoretical spectrum of Ti_2O_3 contains two key features (B and C) seen also in the experimental spectrum. Fig. 5 shows that the theoretical spectra of CeTi_2O_6 and Ce_2TiO_5 are the best models for reproducing the two key features (B and C) of the experimental data. However, as shown by the Ce L_3 -edge spectra [Fig. S2(b)], the local structure of Ce is similar to that in 20GDC, implying that the Ce ions in all Ti-GDC samples in region I are coordinated with eight oxygen atoms, as opposed to the six oxygen atoms in Ce_2TiO_5 . Therefore, the CeTi_2O_6 structure, which contains a similar Ce environment to that of 20GDC, wins (our PCA analysis for Ce L_3 -edge XANES is inconsistent with the mixed Ce environment in region 1, as shown in Figs. S4 and S5), and we identify it as the prevailing model of the local structure of Ti in region I.

3.2. Region II

Region II contains 57%, 65%, 74%, 84% and 88% Ti-GDC samples. According to Fig. 1, the local environment of Ti is octahedral. In contrast to the pre-edge features in the Ti-GDC samples in region I (Fig. S1), the dominant feature in the pre-edge region is the split into A1 and A2 features, as shown in Fig. 6. The positions of the A1, A2 and A3 features are similar to the anatase phase reported by Ke *et al.* (2020), but the intensity of these features is much higher for the Ti-GDC samples in our work. The intensity of the pre-edge features is weak in centrosymmetric environments (Luca *et al.*, 1998), and increases as the environment is distorted. Empirical approaches have been used by Luca *et al.* (1998) to establish correlations between the Ti K pre-edge transitions in anatase- TiO_2 , indicating that the intensity ratio (I_{A1}/I_{A2}) of the Ti K -pre-edge feature A1 to A2 transitions [equivalent peaks of Luca *et al.* (1998) are labeled as A2 and A3, respectively] increases as particle size decreases, as well as the surface-area-to-volume ratio of the particles increasing. Farges *et al.* (1996) demonstrated that the A1 peak is due to the pentacoordinated Ti atoms. Zhang *et al.* (2008) simulated the amorphous nano- TiO_2 structure by utilizing reverse Monte Carlo (RMC) and

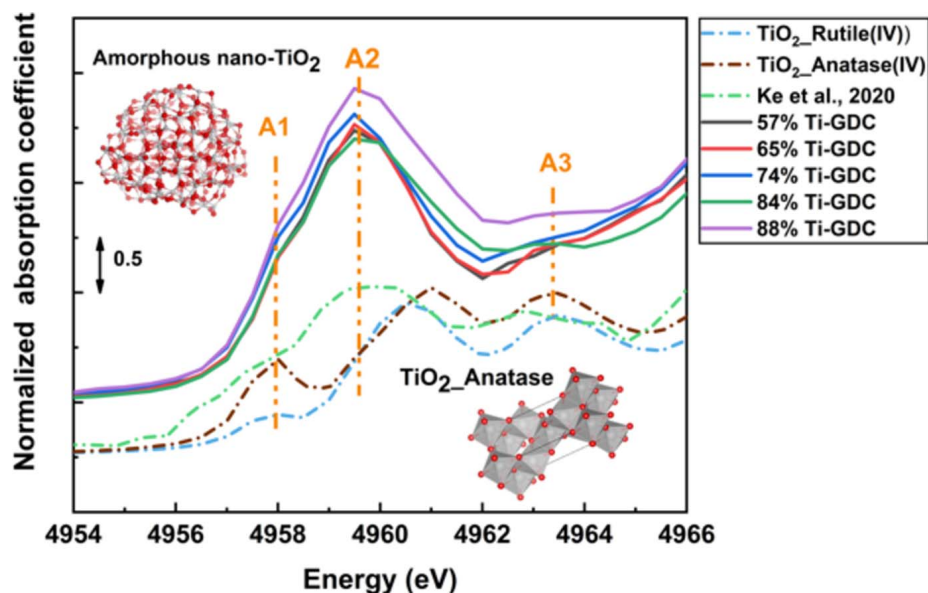
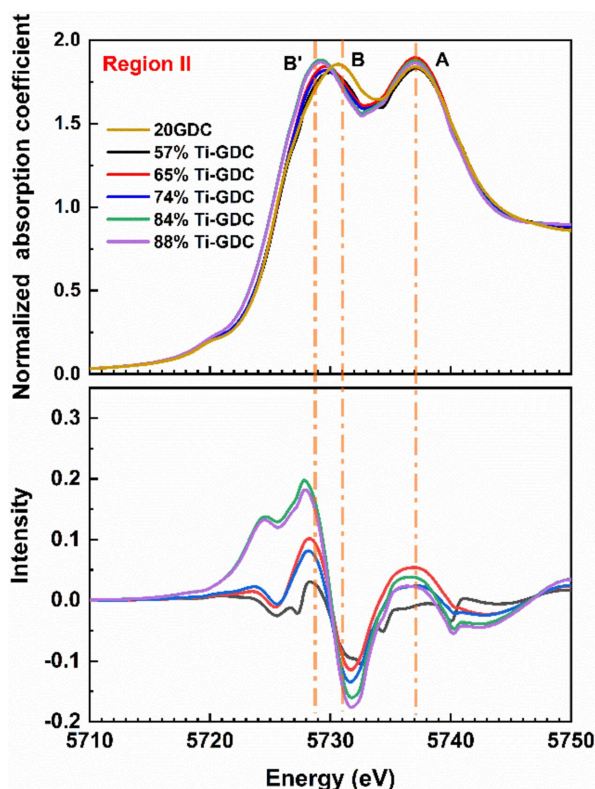


Figure 6

Ti K -pre-edge features for Ti-GDC samples in region II. The distorted anatase Ti K -edge spectrum and reverse Monte Carlo generated amorphous nano- TiO_2 structure are reproduced with permission from Ke *et al.* (2020) [Copyright 2020 American Chemical Society] and Zhang *et al.* (2008) [Copyright 2008 American Physical Society], respectively. The structure of TiO_2 -anatase was generated using information from the Materials Project database (Petousis *et al.*, 2017; Munro *et al.*, 2020; Patel *et al.*, 2019; Jain *et al.*, 2013).

demonstrated that feature A1 was also from the distorted Ti–O octahedra. EXAFS analysis of samples in region II, as shown in Table S2, indicates that the coordination numbers decrease below 6 at high Ti concentration, although the trend is difficult to identify due to the experimental error bars. A reduction of the Ti–O coordination number with respect to the bulk analog (anatase) of 6 is expected in the case of nano-sized TiO_2 , in which the contribution of the under-coordinated Ti atoms on the surface lowers the average coordination number. This effect was also predicted by simulations (Zhang *et al.*, 2008) and observed in several experimental studies (Shkrob *et al.*, 2004; Rajh *et al.*, 2002; Chen *et al.*, 1999). It also does not contradict the conclusion based on the interpretation of the pre-edge intensity (Fig. 1) because the Farges' method was calibrated using bulk-like, standard Ti–O compounds only. Thus, we propose that the disordered nanoscale TiO_2 structure was formed in region II.

As shown in Fig. 7 (top), there are two main Ce L_3 -edge peaks: peak A ($2p f^{0.5d}$ state), which is only expected for Ce^{4+} species, and peak B ($2p f^{1.5d^*}$ state), which originates from the charge transfer from oxygen to the Ce $4f$ orbital (Soldatov *et al.*, 1994; Kossov *et al.*, 2013; Bianconi *et al.*, 1987). $2p$ denotes the empty state in the $2p$ shell and \underline{L} denotes an empty state in the neighboring oxygen orbital. Following the process described by Overbury *et al.* (1998), the 20GDC data were subtracted from each of the Ti-GDC absorption coefficients, and the differences between the Ti-GDC and GDC data are shown in Fig. 7 (bottom). With increasing Ti concentration, there is a progressive decrease in the intensity of peaks B at 5731 eV, but at the same time peak B' is growing, corresponding to the reduction of the Ce species. Hence, both


Figure 7

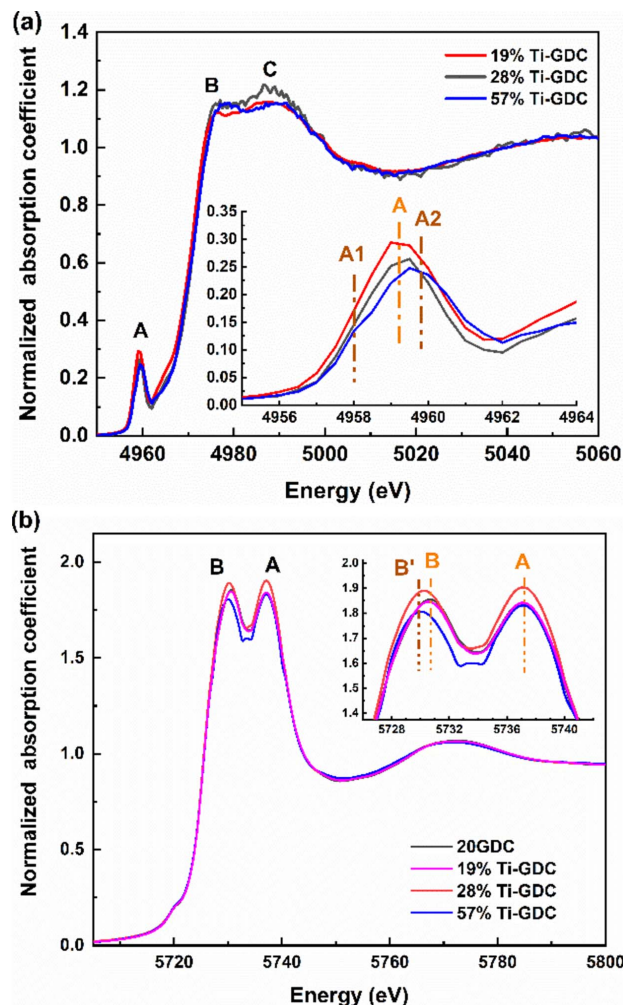
Ce L_3 -edge XANES spectra are shown in the top pane for the 57%, 65%, 74%, 84%, 88% Ti-GDC sample and 20GDC sample. 20GDC data have been subtracted from each spectrum. The difference between the Ti-GDC and 20GDC data is shown in the bottom pane.

Ce^{4+} and Ce^{3+} species are present in the Ti-GDC samples in region II.

3.3. Transition region

According to the results obtained by PCA, the 28% Ti-GDC sample is not identified as either region I or region II. According to Fig. 1, the local environment of Ti is octahedral. As shown in Fig. 8(a), the normalized Ti K -pre-edge XANES spectrum of 28% Ti-GDC is close to that in the 19% Ti-GDC sample, with only one prominent peak rather than the two splitting peaks in 57% Ti-GDC samples. In addition, the intensity of the pre-edge peak A in 28% Ti-GDC is lower than that in the 19% Ti-GDC sample. Moreover, as shown in Fig. 8(b), the position of the peak B of the Ce L_3 -edge XANES spectrum of 28% Ti-GDC is between the 20GDC and the 57% Ti-GDC sample, indicating the coexistence of the Ce^{4+} and Ce^{3+} species. Therefore, the region between region I and region II is transitional between nanoscale cerium titanate structure and phase-segregated disordered titania.

Based on the combination of experimental and theoretical XANES spectroscopy of Ti K - and Ce L_3 -edges and XRD studies, we identified the range of Ti concentrations (from 28% to 88%, using multiple Ti-GDC samples with controlled Ti compositions) in which TiO_x can be detected as a separate region. This result is consistent with the previous work in which 38% Ti in Ti-GDC was found to be electro-chemo-


Figure 8

(a) Normalized Ti K -edge XANES spectra of 28% Ti-GDC and references: 19% Ti-GDC and 57% Ti-GDC. Inset: enlarged pre-edge region. (b) Normalized Ce L_3 -edge XANES spectra of 28% Ti-GDC and references: 20GDC, 19% Ti-GDC and 57% Ti-GDC. Inset: enlarged region of the main peaks.

mechanically active (Makagon *et al.*, 2021). TiO_x with locally disordered octahedral TiO_6 units undergoes rapid oxidation and reduction during ECM coupling. However, ECM devices with the working body consisting of 100% TiO_x show immediate saturation of the ECM response due to a lack of oxygen transport (Mishuk *et al.*, 2019). Hence, the coexistence of the Ce^{4+} and Ce^{3+} species should be the key descriptor for characterizing oxygen diffusion in the ECM actuators. Based on this study we propose that other mixed TiO_2 - CeO_2 systems within the broader range of Ti concentrations can also be ECM-active. For a search of the strongest effect in Ti-GDC composites we propose to investigate the concentrations in the transition region (between 19 and 57 mol% Ti) due to the observed strong local distortion of Ti in the TiO_6 units (hence, capable of generating large local strains) and coexistence of Ce^{4+} and Ce^{3+} (hence, facilitating oxygen transport). Our analysis methodology developed for this material can be used for analyzing a large class of functional mixed metal oxides.

4. Conclusions

The volumetric changes in the two working bodies made by TiO_x/20GDC (Ti-GDC) are essential to generate large mechanical deformation in the ECM actuator. Both XAS and XRD were applied to study the structural changes of Ti-GDC and clarify the local structure of Ti and Ce in Ti-GDC with various Ti concentrations. We detected three different types of local structural units at different Ti concentrations using principal component analysis of XANES spectra and identified the likely structures in each region. In regions I and II, the local structure of Ce species is similar to that in fluorite CeO₂. Nanoscale cerium titanates were formed in region I, while in region II the disordered nano-TiO₂ structure was found. Meanwhile, both Ce⁴⁺ and Ce³⁺ species are present in the Ti-GDC samples in region II. Between regions I and II, there is a transition region containing TiO_x units with strongly distorted TiO₆ octahedra along with coexisting Ce⁴⁺ and Ce³⁺ species. Our results will be helpful for future studies that will aim to link the ECM and other electromechanical effects (e.g. electrostriction) to the local geometric and electronic properties of mixed oxides.

Acknowledgements

This research used beamlines 8-BM and 28-ID-2 of the National Synchrotron Light Source II (NSLS-II), a US DOE Office of Science User Facility operated for the DOE Office of Science by Brookhaven National Laboratory under contract No. DE-SC0012704. Use of the Stanford Synchrotron Radiation Lightsource, SLAC National Accelerator Laboratory, is supported by the US Department of Energy, Office of Science, Office of Basic Energy Sciences under Contract No. DE-AC02-76SF00515. We gratefully acknowledge Dr Yonghua Du for his support of these experiments at the 8-BM beamline, Dr Sanjit Ghose for his support of these experiments at the 28-ID-2 beamline of NSLS-II, and Dr Erik Nelson for his support at the 4-3 beamline of SSRL. We acknowledge support by the Synchrotron Catalysis Consortium funded by the US Department of Energy, Office of Science, Office of Basic Energy Sciences, Grant No. DE-SC0012335. AIF acknowledges support by Weston Visiting Professorship during his stay at the Weizmann Institute of Science.

Funding information

The following funding is acknowledged: National Science Foundation (grant No. DMR-1911592 to Anatoly Frenkel, Junying Li, Yuanyuan Li, Prahlad K. Routh); Binational Science Foundation (Israel) (grant No. 2018717 to Igor Lubomirsky).

References

Ankudinov, A., Rehr, J., Low, J. J. & Bare, S. R. (2002). *J. Chem. Phys.* **116**, 1911–1919.
 Bazuev, G., Makarova, O., Zhilyaev, V. & Shveikin, G. (1976). *Russ. J. Inorg. Chem.* **21**, 1447.
 Bianconi, A., Marcelli, A., Dexpert, H., Karnatak, R., Kotani, A., Jo, T. & Petiau, J. (1987). *Phys. Rev. B*, **35**, 806–812.

Bishop, S., Marrocchelli, D., Chatzichristodoulou, C., Perry, N. H., Mogensen, M. B., Tuller, H. & Wachsman, E. (2014). *Annu. Rev. Mater. Res.* **44**, 205–239.
 Bishop, S. R., Perry, N. H., Marrocchelli, D., Sheldon, B. W., Zuev, A. Y., Tsvetkov, D. S., Santiso, J., Moreno, R., Hull, S. & Nicholas, J. D. (2017). *Electro-chemo-mechanics of Solids*. Springer.
 Chen, L. X., Rajh, T., Jäger, W., Nedeljkovic, J. & Thurnauer, M. C. (1999). *J. Synchrotron Rad.* **6**, 445–447.
 Farges, F., Brown, G. E. & Rehr, J. (1997). *Phys. Rev. B*, **56**, 1809–1819.
 Farges, F., Brown, G. E. Jr & Rehr, J. J. (1996). *Geochim. Cosmochim. Acta*, **60**, 3023–3038.
 Fay, M. J., Proctor, A., Hoffmann, D. P., Houalla, M. & Hercules, D. M. (1992). *Mikrochim. Acta*, **109**, 281–293.
 Frenkel, A. I., Ehre, D., Lyahovitskaya, V., Kanner, L., Wachtel, E. & Lubomirsky, I. (2007). *Phys. Rev. Lett.* **99**, 215502.
 Frenkel, A. I., Feldman, Y., Lyahovitskaya, V., Wachtel, E. & Lubomirsky, I. (2005). *Phys. Rev. B*, **71**, 024116.
 Frenkel, A. I., Kleinfeld, O., Wasserman, S. R. & Sagi, I. (2002). *J. Chem. Phys.* **116**, 9449–9456.
 Gao, Z., Liu, L., Han, X., Meng, X., Cao, L., Ma, G., Liu, Y., Yang, J., Xie, Q. & He, H. (2015). *J. Am. Ceram. Soc.* **98**, 3930–3934.
 Gionco, C., Paganini, M. C., Agnoli, S., Reeder, A. E. & Giamello, E. (2013). *J. Mater. Chem. A*, **1**, 10918–10926.
 Jain, A., Ong, S. P., Hautier, G., Chen, W., Richards, W. D., Dacek, S., Cholia, S., Gunter, D., Skinner, D., Ceder, G. & Persson, K. A. (2013). *APL Mater.* **1**, 011002.
 Jolliffe, I. T. & Cadima, J. (2016). *Philos. Trans. R. Soc. A* **374**, 20150202.
 Kadhim, F. M., Baqer, A. A., Shanan, Z. J. & Tameem, M. K. (2021). *AIP Conf. Proc.* **2402**, 180009.
 Ke, W., Liu, Y., Wang, X., Qin, X., Chen, L., Palomino, R. M., Simonovis, J. P., Lee, I., Waluyo, I., Rodriguez, J. A., Frenkel, A. I., Liu, P. & Zaera, F. (2020). *Nano Lett.* **20**, 6884–6890.
 Kityakarn, S., Worayingyong, A., Suramitr, A. & Smith, M. (2013). *Mater. Chem. Phys.* **139**, 543–549.
 Kossoy, A., Wang, Q., Korobko, R., Grover, V., Feldman, Y., Wachtel, E., Tyagi, A., Frenkel, A. & Lubomirsky, I. (2013). *Phys. Rev. B*, **87**, 054101.
 Kraizman, V. L., Novakovich, A. A., Vedrinskii, R. V. & Timoshevskii, V. A. (1995). *Physica B*, **208–209**, 35–36.
 Li, J., Li, Y., Routh, P. K., Makagon, E., Lubomirsky, I. & Frenkel, A. I. (2021). *J. Synchrotron Rad.* **28**, 1511–1517.
 Luca, V., Djajanti, S. & Howe, R. F. (1998). *J. Phys. Chem. B*, **102**, 10650–10657.
 Luo, S., Nguyen-Phan, T.-D., Johnston-Peck, A. C., Barrio, L., Sallis, S., Arena, D. A., Kundu, S., Xu, W., Piper, L. F., Stach, E. A., Polyansky, D. E., Fujita, E., Rodriguez, J. A. & Senanayake, S. D. (2015). *J. Phys. Chem. C*, **119**, 2669–2679.
 Makagon, E., Li, J., Li, Y., Wachtel, E., Frenkel, A. I. & Lubomirsky, I. (2022). *Solid State Ion.* **379**, 115913.
 Makagon, E., Wachtel, E., Houben, L., Cohen, S. R., Li, Y., Li, J., Frenkel, A. I. & Lubomirsky, I. (2021). *Adv. Funct. Mater.* **31**, 2006712.
 Mishuk, E., Ushakov, A., Makagon, E., Cohen, S. R., Wachtel, E., Paul, T., Tsur, Y., Shur, V. Y., Kholkin, A. & Lubomirsky, I. (2019). *Adv. Mater. Interfaces*, **6**, 1801592.
 Momma, K. & Izumi, F. (2011). *J. Appl. Cryst.* **44**, 1272–1276.
 Munro, J. M., Latimer, K., Horton, M. K., Dwaraknath, S. & Persson, K. A. (2020). *npj Comput. Mater.* **6**, 112.
 Otsuka-Yao-Matsuo, S., Omata, T. & Yoshimura, M. (2004). *J. Alloys Compd.* **376**, 262–267.
 Overbury, S., Huntley, D., Mullins, D. & Glavee, G. (1998). *Catal. Lett.* **51**, 133–138.
 Patel, A. M., Nørskov, J. K., Persson, K. A. & Montoya, J. H. (2019). *Phys. Chem. Chem. Phys.* **21**, 25323–25327.

- Petousis, I., Mrdjenovich, D., Ballouz, E., Liu, M., Winston, D., Chen, W., Graf, T., Schladt, T. D., Persson, K. A. & Prinz, F. B. (2017). *Sci. Data*, **4**, 160304.
- Poumellec, B., Durham, P. J. & Guo, G. Y. (1991). *J. Phys. Condens. Matter*, **3**, 8195–8204.
- Preuss, A. & Gruehn, R. (1994). *J. Solid State Chem.* **110**, 363–369.
- Rajh, T., Chen, L., Lukas, K., Liu, T., Thurnauer, M. & Tiede, D. (2002). *J. Phys. Chem. B*, **106**, 10543–10552.
- Ravel, B. & Newville, M. (2005). *J. Synchrotron Rad.* **12**, 537–541.
- Rehr, J. J. & Albers, R. C. (2000). *Rev. Mod. Phys.* **72**, 621–654.
- Rehr, J. J., Albers, R. C. & Zabinsky, S. I. (1992). *Phys. Rev. Lett.* **69**, 3397–3400.
- Rehr, J. J., Kas, J. J., Prange, M. P., Sorini, A. P., Takimoto, Y. & Vila, F. (2009). *C. R. Phys.* **10**, 548–559.
- Sayers, D. E., Stern, E. A. & Lytle, F. W. (1971). *Phys. Rev. Lett.* **27**, 1204–1207.
- Sethuraman, V. A., Chon, M. J., Shimshak, M., Srinivasan, V. & Guduru, P. R. (2010). *J. Power Sources*, **195**, 5062–5066.
- Shanthakumar, P., Balasubramanian, M., Pease, D. M., Frenkel, A. I., Potrepka, D. M., Kraizman, V., Budnick, J. I. & Hines, W. A. (2006). *Phys. Rev. B*, **74**, 174103.
- Shkrob, I. A., Sauer, M. C. & Gosztola, D. (2004). *J. Phys. Chem. B*, **108**, 12512–12517.
- Soldatov, A., Ivanchenko, T., Della Longa, S., Kotani, A., Iwamoto, Y. & Bianconi, A. (1994). *Phys. Rev. B*, **50**, 5074–5080.
- Srivastava, U. & Nigam, H. (1973). *Coord. Chem. Rev.* **9**, 275–310.
- Swallow, J., Woodford, W., Chen, Y., Lu, Q., Kim, J., Chen, D., Chiang, Y.-M., Carter, W., Yildiz, B., Tuller, H. & Van Vliet, K. J. (2014). *J. Electroceram.* **32**, 3–27.
- Swallow, J. G., Kim, J. J., Maloney, J. M., Chen, D., Smith, J. F., Bishop, S. R., Tuller, H. L. & Van Vliet, K. J. (2017). *Nat. Mater.* **16**, 749–754.
- Tuller, H. L. & Bishop, S. R. (2011). *Annu. Rev. Mater. Res.* **41**, 369–398.
- Wang, X., Fan, F., Wang, J., Wang, H., Tao, S., Yang, A., Liu, Y., Beng Chew, H., Mao, S. X., Zhu, T. & Xia, S. (2015). *Nat. Commun.* **6**, 8417.
- Watanabe, S., Ma, X. & Song, C. (2009). *J. Phys. Chem. C*, **113**, 14249–14257.
- Yamamoto, T. (2008). *X-ray Spectrom.* **37**, 572–584.
- Zhang, H., Chen, B., Banfield, J. F. & Waychunas, G. A. (2008). *Phys. Rev. B*, **78**, 214106.